Research Article | Vol. 29, No. 17 / 16 Aug 2021 / Optics Express 27816
Optics EXPRESS

# Multifunctional and reconfigurable graphene/liquid crystal-assisted asymmetrical Fabry-Pérot cavity for reflected light control

GIOVANNI MAGNO,* MARCO GRANDE, AND ANTONELLA D'ORAZIO

*Dipartimento di Ingegneria Elettrica e dell'Informazione (DIEI), Politecnico di Bari, Via Re David 200, 70126 Bari, Italy*
*giovanni.magno@poliba.it*

**Abstract:** Multifunctional and reconfigurable devices are crucial for compact and smart optoelectronic devices. In this paper, we propose a multifunctional and spectrally reconfigurable asymmetric 1D PhC Fabry-Pérot cavity filled with nematic liquid crystal and bounded by two graphene monolayers. Due to the large number of available degrees of freedom, such a structure can behave as either a notch filter, an absorber, an amplitude modulator, or a phase shifter for the reflected electromagnetic waves. The chemical potential of one or both graphene monolayers can be exploited to modulate the amplitude and phase-shift angle of the reflected electromagnetic waves. Furthermore, all functions are narrowband (1 nm linewidth) and are spectrally tunable over a range of about 200 nm around the working wavelength of 1550 nm by controlling the orientation of the elongated molecules of the liquid crystal. This structure may be advantageously exploited for the realization of optical modulators and beamsteering systems.



## 1. Introduction

There is no denying that photonics has experienced tremendous improvement over the past two decades. In large part, this has been inspired by analogies, mimicking phenomena discovered in other physical systems and translated into the language of photons. The distinctive behavior of electronic waves in conventional electronic insulators have inspired periodically structured artificial photonic media such as photonic crystals as a photonic analogue of conventional electronic insulators [1,2]. Dielectric and metallic photonic crystals (PhCs) and metamaterials are among the cornerstones of optics and photonics today, enabling a plethora of distinct applications: ultra-high Q-factor optical resonators [3,4], biocompatible sensors [5,6], near-field optical tweezers [7,8], slow-light waveguides [9], non-linear optics [10], self-collimation [11], interconnections for photonic circuitry [12], photovoltaics [13,14], etc.

Today, providing a device with multi-functionality and reconfigurability becomes an increasingly important requirement to meet the growing demand for improved compactness and intelligent architectural solutions. Multi-functionality allows a single device to perform a plurality of functions while reconfigurability implies the possibility of modifying the behavior of its individual functions through external control. On the one hand, the former can arise when an abundance of degrees of freedom is found in the same topology, as we have previously shown in the case of self-collimating structures based on 2D mesoscopic PhCs [15–17]. On the other hand, the latter is achieved by exploiting the tunability of its component materials through the harnessing of several physical mechanisms: phase transitions [18], piezoelectricity [19], thermo- [20], electro- [21] and magneto-optical [22] effects, and two-dimensional materials peculiar properties, to name the most common. By far the most celebrated 2D semiconductor, monolayer graphene, exhibits important optical properties, owing to the simplicity of its electronic bands which are gapless Dirac cones near the zero energy [23]. Because of this peculiar band structure, in which

#432166 https://doi.org/10.1364/OE.432166
Journal © 2021 Received 21 May 2021; revised 1 Jul 2021; accepted 4 Jul 2021; published 13 Aug 2021

Optics EXPRESS

conduction and valence bands touch at the Dirac points, electrons behave as massless Dirac fermions, showing an extremely high mobility [24]. Monolayer graphene exhibits reconfigurable conductivity via chemical or electrostatic doping, for example by applying a voltage between the graphene and an electrode separated by a thin insulator, resulting in a change in the number of electrons or holes (which depends on the applied bias) available for conduction. In visible and near-infrared spectral domain, coupling graphene monolayers to optical high-Q resonant structure leads to light-graphene interaction enhancement. In particular, enhanced absorption can be achieved under critical coupling in interferometric configurations, such as Fabry-Pérot resonators [25], and field distribution engineering [26–28] by means of the so called coherent perfect absorption (CPA) mechanism [29,30].

In this manuscript, we present an innovative structure that combines the paradigms of multifunctionality and reconfigurability through the joint use of a 1D PhC Fabry-Pérot asymmetric cavity, whose defect, filled with nematic liquid crystal, is bounded by two graphene monolayers. 1D PhCs, compared to their higher-dimensional counterparts, offer the advantages of a simpler fabrication process and, generally, greater simplicity in understanding the physical phenomena involved. In such structures, perfect and narrowband absorption has been already demonstrated in presence of a single graphene monolayer placed at the center of the cavity defect [31,32]. The proposed structure has many degrees of freedom (geometrical parameters, chemical potentials of graphene layers, liquid crystal orientation) which can be exploited to control, over a very narrow linewidth, the amplitude (via absorption) and phase of the reflected electromagnetic wave and to tune the bandwidth of such functions over a wide spectral range at telecommunication wavelengths. We will numerically show that it is possible to identify some important reconfigurable optical functions that the proposed structure may allow to be implemented: amplitude modulation, notch filter and phase shifter. Figure 1 shows a sketch of such spectrally reconfigurable optical functions.

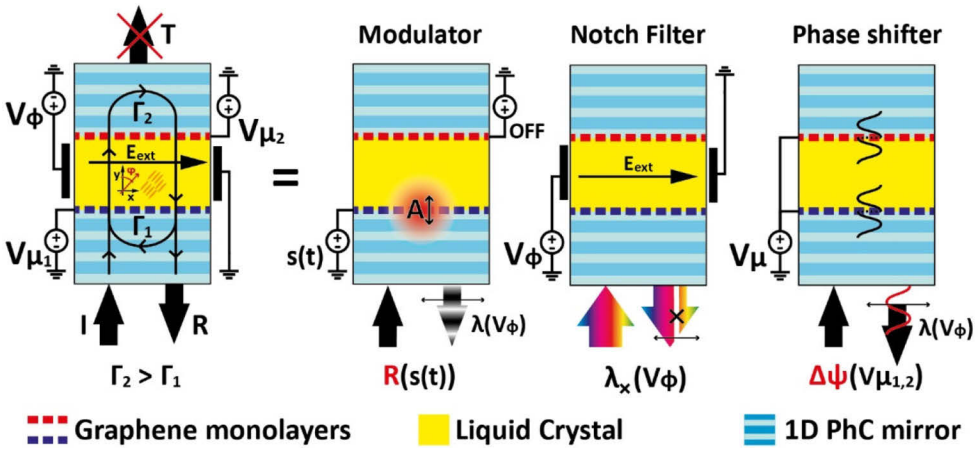


**Fig. 1.** Schematic diagram showing mechanisms, control inputs enabling reconfigurability (the two chemical potentials of the two graphene layers and the external electric field applied on the liquid crystal contained in the cavity defect) and functionalities of the proposed structure. The asymmetric cavity (Γ1 and Γ2 represent the reflection coefficients of the lower and the upper 1D PhC mirrors, respectively) ensures that almost the whole incident power is reflected or absorbed. On the one hand, the two graphene layers bounding the cavity defect act as narrow-band absorbers and phase shifters based on their chemical potentials. On the other hand, the external electric field applied on the liquid crystal contained in the cavity defect allows the optical length of the cavity to be changed by electrooptic effect, which results in a spectral shift of the resonance that ensures spectral reconfigurability.

Optics EXPRESS

The manuscript will be structured as follows. Firstly, (i) in the Structure and methods section the proposed device will be presented and the geometric parameters and material properties (in particular, the angular properties of the liquid crystal and the conductivity of the graphene monolayer), essential to numerical modeling, will be detailed. Furthermore, the 1D PhC mirror design and cavity defect dimensioning will be detailed. Then, (ii) in the Results and discussion section to facilitate the understanding of the mechanisms underlying the proposed structure, the effects of altering the two graphene monolayers' chemical potentials and the liquid crystal elongated molecule orientation will then be decoupled and presented separately. Thus, having fixed the orientation of the liquid crystal and the chemical potentials, (a) the effect of the number of periods constituting the mirrors delimiting the cavity will first be studied to numerically identify the quasi-CPA condition that will result in an almost complete absorption of the incident radiation. With the number of periods fixed, (b) the effect of varying the chemical potentials of the two graphene monolayers is then presented. This is done in terms of both absorbance and spectral shift of the localized optical mode resonance peak of the cavity. This will help to identify the ranges of chemical potentials in which certain particularly convenient regions of operation occur. (c) The response of the device to the change in orientation of the liquid crystal by an external static electric field will then be presented; (d) the multifunctionality and reconfigurability of the proposed structure and its application as a concrete device will finally be discussed in final part of the result section. (iii) Potential applications and developments will be discussed in the conclusions.

## 2. Structure and methods

Figure 2(a) shows a sketch of the envisaged multifunctional structure: a $t_{LC}$ wide cavity defect, filled with a nematic liquid crystal (NLC) of type E7, is surrounded by two 1D PhC mirrors arranged specularly at its sides. E7 mixture was chosen for its high positive birefringence ($\Delta n \sim 0.185$ near the working wavelength 1.55 μm), low viscosity, good chemical stability and commercial availability. The PhC mirror is composed of two layers of different dielectric materials, $Ta_2O_5$ and $SiO_2$, of thicknesses $t_1$ and $t_2$, respectively, having period $p$. These materials were chosen for their low losses and because they provide sufficiently high refractive index contrast in the spectral region of interest. Each PhC mirror terminates on a graphene monolayer ($GL_1$ and $GL_2$, indicated by the two dashed red and blue lines in Fig. 2(a)), of negligible thickness, on which a small thickness $t_p = 50\ nm$ of polyimide (PI2723 [33]) is deposited (indicated by the two pale orange layers in Fig. 2(a)). The latter serves as an orientation layer for the NLC that fills the cavity defect. All numerical simulations presented in this manuscript are performed by means of the Finite Element Method [34].

NLCs behave as anisotropic positive uniaxial crystals with the optical axis oriented in the same direction as the elongated molecules. If the polarization of the wave travelling through the NLC is orthogonal (parallel) with respect to the optical axis, the phase velocity experienced will be $c/n_o$ ($c/n_e$), being $c$ the speed of light in vacuum and $n_o$ and $n_e$ the ordinary and the extraordinary refractive indexes of the NLC. Here, we will excite the structure with a plane wave impinging from the input port, with the wave vector $\mathbf{k} = k_y\mathbf{u_y}$ and polarization so that $\mathbf{E} = E_x\mathbf{u_x}$, being $\mathbf{u_x}$ and $\mathbf{u_y}$ unitary vectors along the x and y directions, respectively. As depicted in Fig. 2(a), we assume $\phi$ as the angle that the optical axis of the NLC forms with the $y$-axis in the [$xy$]-plane. In the unbiased state, NLC molecules are assumed to be oriented along the $y$-axis and the relative permittivity tensor is $[\varepsilon_{LC}] = [{n_o}^2, 0, 0; 0, {n_e}^2, 0; 0, 0, {n_o}^2]$. By applying a static electric field by means of external electrodes is it possible to reorient the elongated molecules of the LC and thus to modify the angle $\phi$. By rotating the relative permittivity tensor around the $z$-axis by one angle

Optics EXPRESS

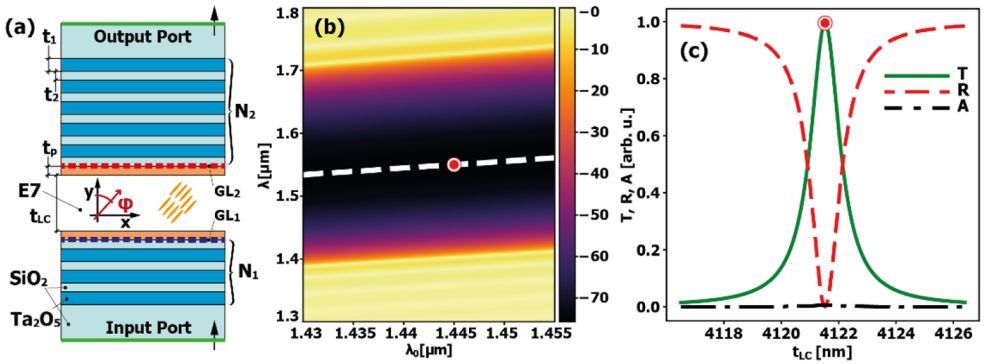


**Fig. 2.** (a) – Sketch of the proposed structure. The two black arrows indicate the propagation direction. (b) Logarithm of the transmittance of a 30 periods-long 1D PhC (same type as that constituting the cavity's surrounding mirror) as a function of the wavelength and of the design parameter $\lambda_0$. The dashed white line represents the locus of the transmittance minimum. As for the red marker, it identifies the value of the $\lambda_0$ design parameter, equal to 1445 nm, for which the transmittance minimum occurs at 1550 nm. (c) Transmittance (green solid curve), reflectance (red dashed curve), and absorbance (black dash-dot curve) as a function of the thickness $t_{LC}$ of the cavity defect, calculated in the absence of the two graphene layers.

$\phi$, we obtain:

$$[\varepsilon_{LC}] = \begin{bmatrix} n_o^2\cos^2\phi + n_e^2\sin^2\phi & (n_o^2 - n_e^2)\sin\phi\cos\phi & 0 \\ (n_o^2 - n_e^2)\sin\phi\cos\phi & n_e^2\cos^2\phi + n_o^2\sin^2\phi & 0 \\ 0 & 0 & n_o^2 \end{bmatrix} \tag{1}$$

which implies that the dispersion equation for the extraordinary waves is:

$$k_y^2(n_e^2\cos^2\phi + n_o^2\sin^2\phi) = k_0^2 n_e^2 n_o^2 \tag{2}$$

where $k_0$ is the vacuum wavenumber. Finally, the refractive index experienced by the extraordinary wave travelling along the $y$-direction for an arbitrary orientation of the NLC optical axis is:

$$n_{LC} = \sqrt{\frac{n_e^2 n_o^2}{n_o^2\sin^2\phi + n_e^2\cos^2\phi}} \tag{3}$$

where $n_o$ and $n_e$ have been modeled as dispersive and lossy after [35]. Additionally, to account for E7 losses we add a dispersive imaginary part $\kappa_{lc}$ modeled after [36].

$Ta_2O_5$ layers have been modelled as a dispersive, lossy material with index $n_{Ta2O5}$ after [37] and $SiO_2$ layers as a dispersive, lossless material with index $n_{SiO2}$ after [38,39]. Their thicknesses were chosen so that the forbidden band of the 1D PhC is centered around 1550 *nm*. This was done by setting $t_1 = \lambda_0/(4n_{Ta2O5})$ and $t_2 = \lambda_0/(4n_{SiO2})$, where $\lambda_0$ is a design parameter. Figure 2(b) shows the transmittance of a 1D PhC with 30 periods as a function of wavelength and design parameter $\lambda_0$. From the same figure we observe that the minimum transmittance occurs at 1550 *nm* when $\lambda_0 = 1445$ *nm*. Therefore, the thicknesses $t_1$ and $t_2$ are set equal to 173 *nm* and 250 *nm*, respectively.

Polyimide layers have been modelled as a dispersionless, lossy material with $n = 1.678 + j10^{-4}$ [33]. The two graphene monolayers, placed between one end of the photonic crystal mirrors and

Optics EXPRESS

the polyimide layer, were modeled as a surface current density $\mathbf{J}=\sigma E_x \mathbf{u_x}$ [40], where $\sigma$ is the graphene monolayer isotropic conductivity [*S*], modelled by means of the Kubo model [23,41,42] as the sum of an intraband ($\sigma_i$) and an interband ($\sigma_o$) term in absence of any external magnetic field. In the mid-infrared spectral regime, the intraband term can be written in a closed form as:

$$\sigma_i = \frac{je^2}{\pi\hbar^2(\omega + j\Gamma)} \int_{-\infty}^{\infty} |\xi| \frac{df_F(\xi)}{d\xi} d\xi = \frac{e^2 k_B T}{j\pi\hbar^2(\omega + j\Gamma)} 2 \ln\left[2\cosh\left(\frac{\mu_{c,n}}{2k_B T}\right)\right] \tag{4}$$

where $e$, $\hbar$, $\mu_{c,n}$, $\omega$, $\Gamma$, $k_B$, and T are the electron charge, the reduced Planck constant, the chemical potential of the $n$-th graphene monolayer, the angular frequency, the energy independent phenomenological scattering rate, the Boltzmann's constant, and the temperature, respectively. $f_F(E)=[1+\exp((E-\mu_{c,i})/(k_B T)]^{-1}$ is the Fermi-Dirac distribution. The interband term can be written as:

$$\sigma_o = \frac{e^2(\omega + j\Gamma)}{j2\pi\hbar^2} \int_0^{\infty} \left[\frac{\tanh\left(\frac{\xi-\mu_{c,n}}{2k_B T}\right) + \tanh\left(\frac{\xi+\mu_{c,n}}{2k_B T}\right)}{(\omega + j\Gamma)^2 - 4\left(\frac{e}{\hbar}\right)^2}\right] d\xi \tag{5}$$

which we solve through numerical integration as suggested in [43] to avoid pole singularity. We assume $\Gamma = 0.66\ meV$ [44] for both the two graphene monolayers and a room temperature $T = 300\ K$. The real and the imaginary part (indicated with one and two apices, respectively) of $\sigma$, $\sigma_i$, and $\sigma_o$ are plotted in Fig. 3 for several combinations of wavelengths and chemical potentials. It is worth noticing that, in this parameter range $\sigma_i$' is always negligeable and $\sigma_o$' reaches the limiting value $e^2/2h = 60.85\ \mu S$ for smaller wavelengths. The electron-phonon coupling that may occur in the presence of a polar substrate has been neglected in the expression of monolayer graphene conductivity.

The cavity defect thickness $t_{LC}$ was chosen to maximize transmittance without penalizing feasibility. Figure 2(c) shows the transmittance, the reflectance, and the absorbance of the entire

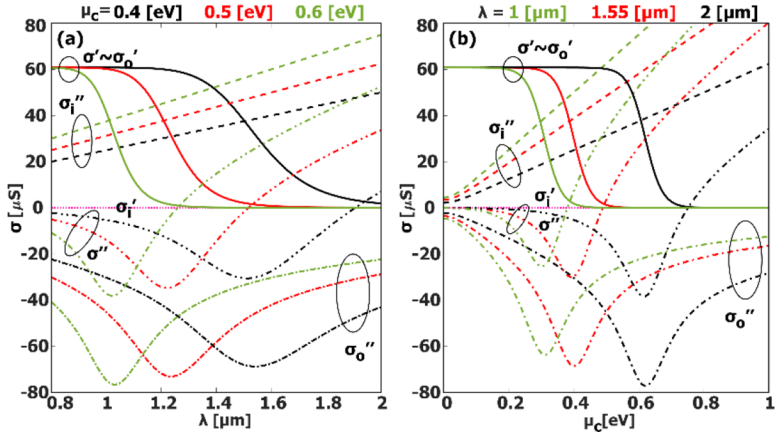


**Fig. 3.** (a) Real ($\sigma$') and imaginary ($\sigma$'') part of the total conductivity (continuous and dashed double-dot curves, respectively), real ($\sigma_o$') and imaginary ($\sigma_o$'') part of the inter-band term of conductivity (continuous and dashed-dot curves, respectively), and real ($\sigma_i$', here negligible) and imaginary ($\sigma_i$'') part of the intra-band term of conductivity (the magenta dotted curve and dashed curves, respectively) as a function of wavelength for three different values of chemical potential (0.4, 0.5, and 0.6 *eV* corresponding to black, red, and green curves, respectively). (b) Same quantities calculated as a function of chemical potential for three different values of wavelength (2, 1.55, and 1 μ*m* corresponding to the black, red, and green curves, respectively).

Optics EXPRESS

structure calculated when the number of periods $N_1$ and $N_2$, constituting the lower and upper PhC mirrors, are both equal to 10 and $t_{LC}$ varies from 4115 to 4125 *nm* (without the two graphene layers). In the absence of graphene monolayers and due to the sole Fabry-Pérot interferometer with low losses materials, the transmittance maximum of about 99.5% (corresponding to a reflectance and absorbance of about 0.01% and 0.49%, respectively) occurs at 1550 *nm* for $t_{LC} \approx$ 4121.5 *nm*.

## 3. Results and discussion

In this section, we shed light on the mechanism that provides reconfigurability and multifunctionality to the structure under investigation. For simplicity and to decouple the effects of the graphene monolayer chemical potential variation from those due to the liquid crystal elongated molecules orientation, at first the study of the cavity will be conducted by enforcing $\phi = 0$, so that $n_{LC} = n_o$. Furthermore, due to the abundance of degrees of freedom, we will limit our analysis only to the excitation that impinges in the normal direction with respect to the input port surface.

Firstly, to maximize the interaction of the cavity optical mode with the two-graphene monolayer, the number of $N_1$ and $N_2$ periods, constituting the lower and upper PhC mirrors bounding the cavity defect, will be varied to identify the quasi-CPA condition that will result in an almost complete absorption of the incident radiation. The two chemical potentials will also be varied, and the effect of these parameters will be observed in terms of transmittance, reflectance, and absorbance in the spectral domain of interest. We start by fixing $N_2 = 15$, $\mu_{c,1} = 0$ *eV* and $\mu_{c,2} = 1$ *eV*, while varying $N_1$ from 3 to 15. It is worth noticing that, as it can be observed by inspecting Fig. 3(b), near 1550 *nm*, when $\mu_{c,i}$ is equal to 0 and 1 *eV*, σ reaches 60.85-j3.52 $\mu S$ and 0.01-j16.46 $\mu S$. With these settings, the lower graphene monolayer will act as a much more effective absorber (achieving an absorbance per single pass of the incident plane wave through it close to 2.3%) than the upper graphene monolayer. Figure 4(a,b) shows the reflectance and the absorbance as a function of the wavelength and $N_1$, respectively. In Fig. 4(b) we observe that there is always an absorbance peak around 1550 *nm* that reaches its highest value of about 98.76% for $N_1 = 7$ and at $\lambda = 1550.2$ *nm* (as shown in Fig. 4(c)). To this absorbance peak, a dip of the reflectance is found, with the lowest value of about 0.66% (as shown in Fig. 4(a)), which implies a transmittance of about the 0.58%. Figure 4(c), shows the transmittance, the reflectance, and the absorbance curves when $N_1 = 7$, $N_2 = 15$, values that will remain fixed henceforth in the manuscript. It is worth remarking that by further increasing the number of periods of the upper mirror beyond $N_2 = 15$, the absorbance does not increase significantly.

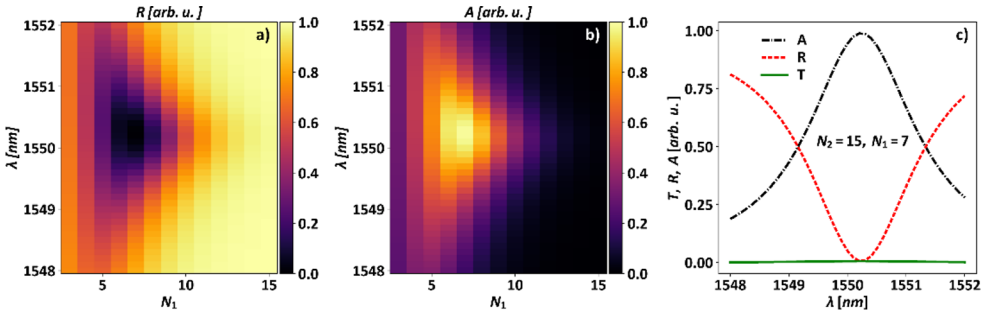


**Fig. 4.** Maps of (a) reflectance and (b) absorbance as a function of wavelength and $N_1$, when $N_2$=15, $\mu_{c,1} = 0$ *eV*, and $\mu_{c,2} = 1$ *eV*. (c) Transmittance (green solid curve), reflectance (red dashed curve), and absorbance (black dash-dot curve) as a function of the wavelegth when $N_1$=7, $N_2$=15, $\mu_{c,1} = 0$ *eV*, and $\mu_{c,2} = 1$ *eV*.

Optics EXPRESS

Having fixed all geometric parameters, we analyzed the effect of the variation of both the chemical potentials. It is worth pointing out that the actual bias values to be applied in order to modify the chemical potential depend on the adopted graphene gating scheme. Figures 5(a,b) show the (a) absorbance and the (b) reflectance maps (at resonance) as a function of $\mu_{c,1}$ and $\mu_{c,2}$ from 0 to 1 *eV*. This figure reveals that the effect of the two chemical potentials is essentially the same, despite the asymmetry of the cavity. On inspection of Figs. 5(a,b), it is possible to distinguish six different regions, which are identified by a numbered label and delimited by dashed green horizontal and vertical lines. On the one hand, within the regions labeled as (1), which occur when one of the chemical potentials is less than or equal to 0.35 *eV* and the other greater than or equal to 0.55 *eV*, the absorbance reaches its highest values, between 98.6% and 99.3%, while the corresponding reflectance and transmittance remain lower than 1%. A similar constant behavior of the absorbance is found in regions labeled (3) and (6): in region (3), when both the chemical potentials are less than or equal to 0.35 *eV*, the absorbance shows values between about 84% and 85% (while the reflectance and the transmittance show values of about 15% and 0.25%, respectively), whereas in region (6), occurring when both the chemical potentials are greater than or equal to 0.55 *eV*, the absorbance reaches its lowest values, between about 1.6% and 5% (while the reflectance ranges between 92.5% and 95.7% and the transmittance show values of about 2.6%). The maximum and minimum transmittance, reflectance, and absorbance values in the operating regions labeled 1, 3, and 6 are summarized in Table 1. On the other hand, in regions labeled as (2), whereby $\mu_{c,1}$ ($\mu_{c,2}$) is between 0.35 and 0.55 *eV* and $\mu_{c,2}$ ($\mu_{c,1}$) is less than 0.35 *eV*, the absorbance increases by increasing $\mu_{c,1}$ ($\mu_{c,2}$) and is almost constant with respect to $\mu_{c,2}$ ($\mu_{c,1}$). An opposite trend is found in regions labeled (4) occurring when $\mu_{c,1}$ ($\mu_{c,2}$) is between 0.35 and 0.55 *eV* and $\mu_{c,2}$ ($\mu_{c,1}$) is greater than 0.55 *eV*, where the absorbance decreases for increasing $\mu_{c,1}$ ($\mu_{c,2}$) and is almost constant with respect to $\mu_{c,2}$ ($\mu_{c,1}$). Finally, the absorbance (as well as the reflectance and the transmittance) shows a saddle point in region (5), whereby both the chemical potential values are between 0.35 and 0.55 *eV*.

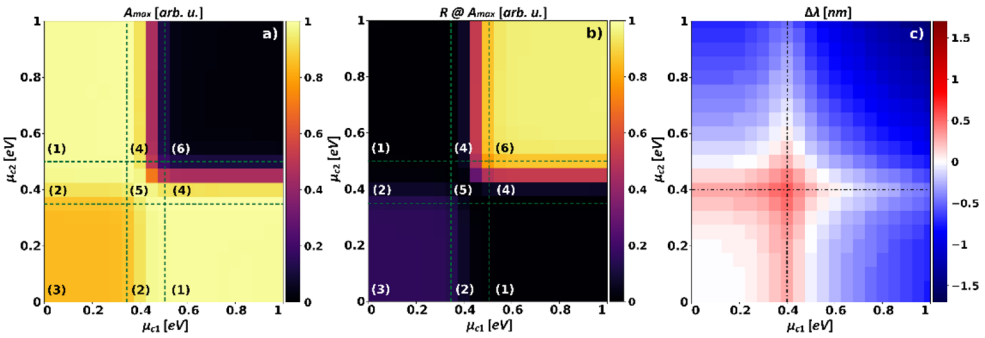


**Fig. 5.** Maps of (a) the absorbance at resonance, (b) the reflectance at resonance, and of (c) the resonance spectral peak shift with respect to 1.55 $\mu m$ as a function of both the chemical potential $\mu_{c,1}$ and $\mu_{c,2}$ varying from 0 to 1 *eV*. In (a,b) green dashed lines highlight the chemical potential values of 0.35 and 0.55 *eV*. In (c) black dash-dotted lines highlight the chemical potential value of 0.4 *eV*.

Figure 5(b) depicts the spectral shift with respect to 1550 *nm* of the absorbance peak as a function of the chemical potentials of the two graphene monolayers. As both $\mu_{c,1}$ and $\mu_{c,2}$ increase from 0 to 0.4 *eV*, the resonance slightly redshifts of about 0.55 *nm*, value that is reached when both the chemical potentials are 0.4 *eV*. For increasing values of both $\mu_{c,1}$ and $\mu_{c,2}$ over 0.4 *eV*, the resonance blueshifts of about 1.75 *nm*. Therefore, the total resonance wavelength shift range is roughly 2.3 *nm*.

Optics EXPRESS

**Table 1. Maximum and minimum transmittance, reflectance, and absorbance values in regions 1, 3, and 6.**

| Regions | $\mu_{c,1}$ *[eV]* | $\mu_{c,2}$ *[eV]* | $T_{min}$ [%] | $T_{max}$ [%] | $R_{min}$ [%] | $R_{max}$ [%] | $A_{min}$ [%] | $A_{max}$ [%] |
|---|---|---|---|---|---|---|---|---|
| 1 | ≤0.35 | ≥0.55 | 0.5 | 0.6 | 0.4 | 0.8 | 98.6 | 99.3 |
| 1 | ≥0.55 | ≤0.35 | 0.5 | 0.6 | 0.4 | 0.8 | 98.6 | 99.3 |
| 3 | ≤0.35 | ≤0.35 | 0.24 | 0.25 | 14.9 | 15.7 | 84.0 | 84.8 |
| 6 | ≥0.55 | ≥0.55 | 2.57 | 2.64 | 92.5 | 95.7 | 1.6 | 4.9 |

Following the analysis performed on Fig. 5 and for ease of explanation, henceforth we will call one of the two graphene monolayers as the "control" layer and the remaining one as the "tuning" layer. A layer will be in the ON (OFF) state if its chemical potential is less than or equal to (greater than or equal to) the critical value of 0.35 *eV* (0.55 *eV*). Figure 6 demonstrates that the device can be used as a reflection modulator, when the working wavelength is close to the cavity resonance. On the one hand, when the control layer is in the ON state while the tuning one is in the OFF state, we lie within one of the two regions (1) identified in Fig. 6(a,b), in which the absorbance is maximum and the reflectance minimum (note that the transmittance is <0.6%). It is worth noting that when the tuning layer is in the OFF state, the cavity resonance blueshifts for increasing chemical potential. This adds a degree of freedom that allows finetuning of the spectral position of the resonance. On the other hand, when control and tuning layers are both in the OFF state (and we lie within the regions (6) identified in Fig. 6(a,b)) the absorbance decreases, and the reflectance increases to values close to unity. It is worth mentioning that Figs. 6(d-f), in which the control monolayer is in its OFF state, describe very well the case in which the tuning layer is completely removed from the device: although it is always possible to achieve the modulation function, in this case, we lose the convenient finetuning degree of freedom.

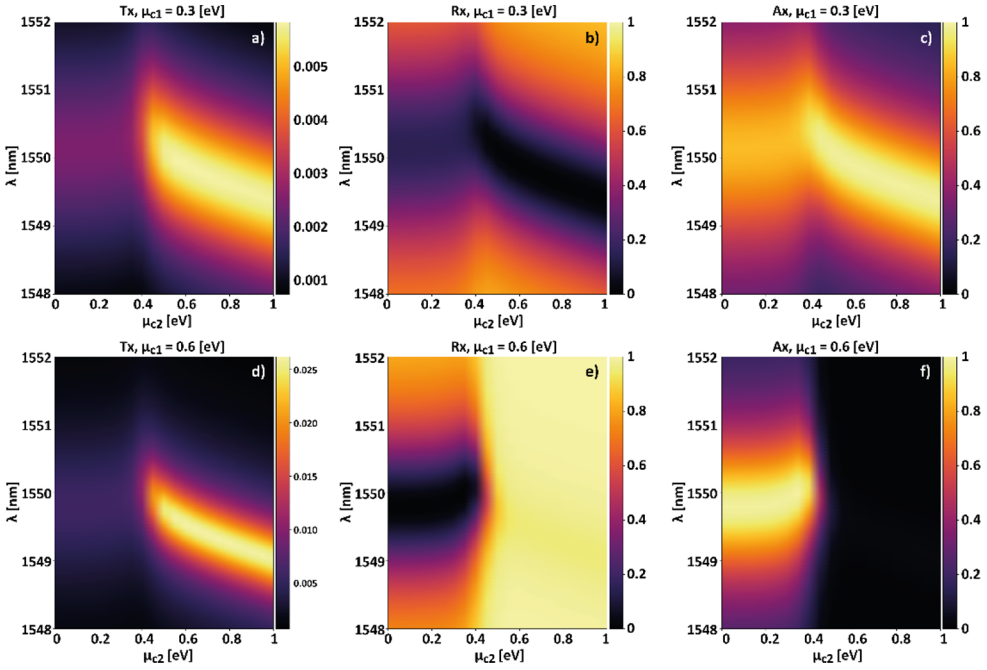


**Fig. 6.** Maps of (a)(b) transmittance, (b)(e) reflectance and (c)(f) absorbance as a function of the wavelength and of the chemical potential $\mu_{c,2}$ when $\mu_{c,1}$ is (a)(b)(c) 0.3 and (d)(e)(f) 0.6 *eV*.

Optics EXPRESS

Finally, Fig. 7 shows that it is possible to exploit the $\phi$ angle, which models the orientation with respect to the y-axis of the elongated particles of the liquid crystal filling the cavity, as a reconfigurability degree of freedom that allows the resonance of the cavity to be tuned along a wide spectral range of about 200 *nm* centred around the design wavelength. Figure 7(a) shows the absorbance map as a function of wavelength (1400 *nm* < λ < 1700 *nm*) and of the $\phi$ angle (between 0 and π/2 radians), when the control and tuning layers operate in the ON and OFF states, respectively. In the observation window, for $\phi = 0$ *rad*, we find 3 resonance peaks (at 1432.5, 1549.9, 1688.7 *nm*, corresponding to absorbances of 77.9%, 99%, and 61.2%, respectively) corresponding to the cavity modes that we term (n-1), n, and (n+1). As the $\phi$ angle increases, the resonances redshift consistently with the refractive index $n_{LC}$ that increases. When $\phi$ exceeds the value of 0.41 *rad*, the (n+1)-th mode goes beyond the observation window and only two modes remain until $\phi$ reaches the value of 0.91 *rad*, where a new mode (which we call the (n-2)-th mode) enters the observation window.

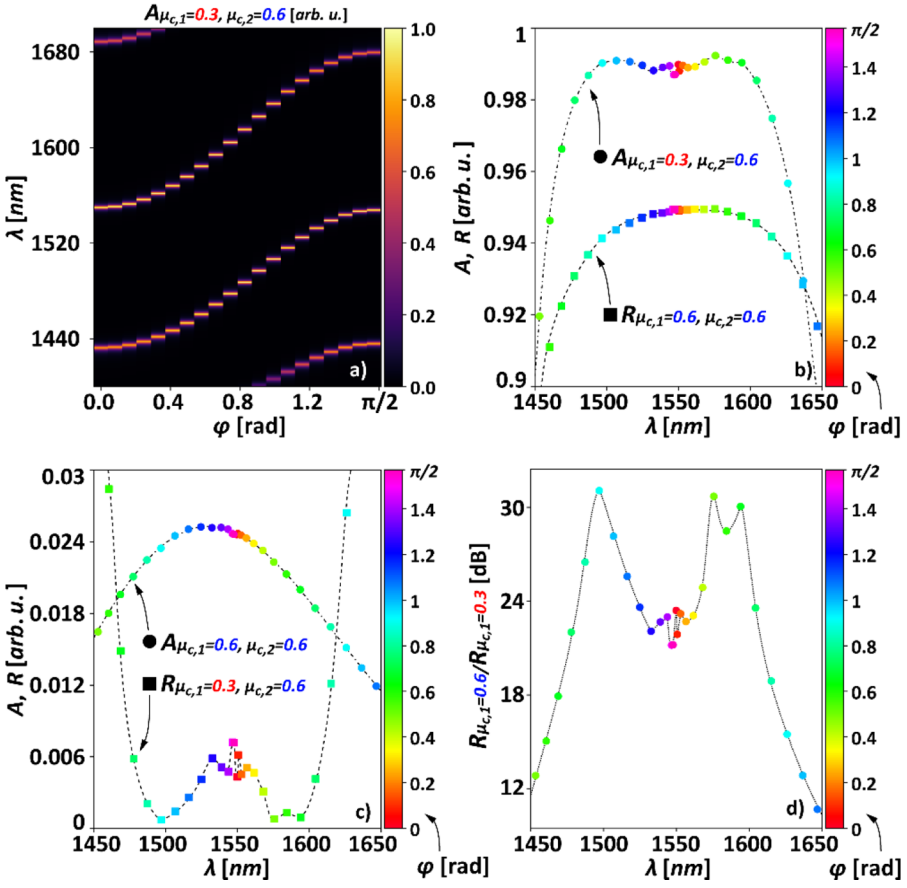


**Fig. 7.** (a) Map of absorbance as a function of the wavelength and of the liquid crystal optical axis angle ϕ, when $\mu_{c,1} = 0.3$ eV and $\mu_{c,2} = 0.6$ eV. (b)(c) Absorbance and reflectance versus wavelength. In (b), the absorbance (reflectance) is calculated when $\mu_{c,1} = 0.3$ eV and $\mu_{c,2} = 0.6$ eV ($\mu_{c,1} = 0.6$ eV and $\mu_{c,2} = 0.6$ eV). In (c), the absorbance (reflectance) is calculated when $\mu_{c,1} = 0.6$ eV and $\mu_{c,2} = 0.6$ eV ($\mu_{c,1} = 0.3$ eV and $\mu_{c,2} = 0.6$ eV). (d) Logarithm of the ratio between the reflectance calculated when $\mu_{c,1} = 0.6$ eV to the reflectance calculated when $\mu_{c,1} = 0.3$ eV (in both cases $\mu_{c,2} = 0.6$ eV). In (b)(c) and (d), the quantities are displayed at the resonances and as a function of the angle ϕ (the value of which is indicated by the colorbar).

Optics EXPRESS

As $\phi$ increases beyond this value, the (n-2)-th, (n-1)-th, and n-th modes continue to shift towards the red until they reach the maximum value of $\phi$ equal to $\pi/2$ radians, where the 3 peaks are positioned at 1435.9, 1547.7, and 1679.7 *nm* (which correspond to absorbance values of 81.1%, 98.7% and 69.1% respectively). Therefore, the n-th and (n-1)-th modes allow to cover, in an almost continuous way the spectral range from 1432.5 *nm* to 1679.7 *nm*. Figure 7(b,c) shows the values of absorbance and reflectance at resonance against wavelength as the $\phi$ angle varies (indicated by the color of the markers and the colorbar) when the tuning layer is in the OFF state. When the control layer is in the ON state, the absorbance is maximum (see Fig. 7(b), while the reflectance is minimum (see Fig. 7(c)). Conversely, when the control layer is in the OFF state, the absorbance is minimum (see Fig. 7(c), while the reflectance is maximum (see Fig. 7(b)). Finally, Fig. 7(d) shows the ratio between the reflectance with the control layer in OFF state and that with the control layer in ON state (in dB), which represents the extinction ratio of the modulation function. We note that in the spectral range 1477 *nm* $< \lambda <$ 1604 *nm* the extinction ratio is greater than 21.8 *dB* and reaches maximum values of 31 and 30.7 *dB* for lambda equal to about 1497 *nm* 1576 *nm*, respectively.

In a nutshell, if the biases of the control and tuning layers are kept fixed so that the first is in the ON state and the second in the OFF state, the structure behaves as a spectrally reconfigurable reflectance notch filter (selective absorber) as the angle $\phi$ changes. On the other hand, when the control layer is switched between ON and OFF states in time, the structure acts as a spectrally reconfigurable narrowband reflectance modulator. In both functions, the absorbed spectral linewidth is about 1 *nm*, with spectral reconfigurability of about 200 *nm* around the working wavelength of 1550 *nm*, achieved through the action of the liquid crystal.

In addition to these two functions, we will now highlight that the structure can also behave as a spectrally tunable phase shifter in reflection. Figure 8(a,b) shows either (i) the phase $\psi_{\mu c,1,\mu c,2}$ of the scattering coefficient $S_{11}$ (reflection coefficient), which represents the phase shift between the incident and reflected waves when $\mu_{c,1}$ and $\mu_{c,2}$ are specified, and (ii) the corresponding reflectance, as the biases of the control and tuning layers are varied. In particular, Fig. 8(a) and Fig. 8(b) show $\psi_{\mu c,1,\mu c,2}$ when the control layer is placed in the ON ($\mu_{c,1} = 0.3$ *eV*) and OFF ($\mu_{c,1} = 0.6$ *eV*) states, respectively, while the tuning layer is in the OFF state and its chemical potential $\mu_{c,2}$ is varied between 0.6 and 1 *eV*. In Fig. 8(b) the case when $\mu_{c,1}$=$\mu_{c,2} = 1$ *eV* is additionally shown.

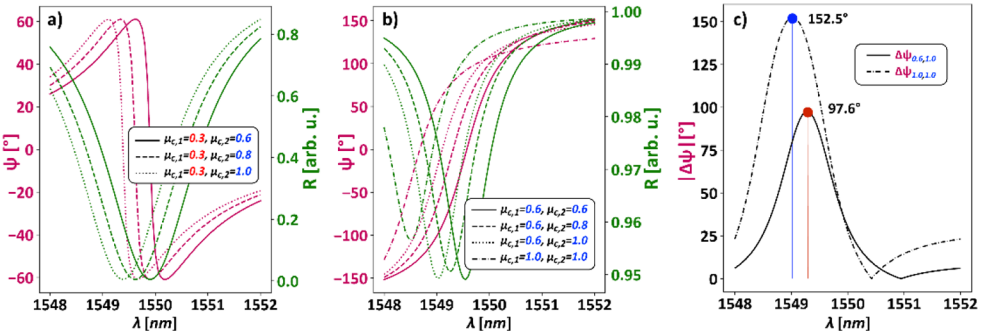


**Fig. 8.** (a),(b) angle of the $S_{11}$ coefficient (values on the left ordinate-axis, with magenta lettering) and reflectance (values on right ordinate-axis, with green lettering) versus wavelength, calculated when (a) $\mu_{c,1}$ is in the ON state while $\mu_{c,2}$ is in the OFF state, and when (b) $\mu_{c,1}$ and $\mu_{c,2}$ are both in the OFF state. It is worth to remark that in the last case the reflectance is always greater than 95% in the observation spectral range (corresponding to insertion losses lower than −0.23 dB). (c) Absolute value of the phase shift difference when $\mu_{c,1} = 0.6$ *eV* and $\mu_{c,2}$ is raised to 1 *eV* (black solid curve) and when both $\mu_{c,1}$ and $\mu_{c,2}$ are raised to 1 *eV* (black dash-dotted curve).

Optics EXPRESS

When the control layer is in the ON state, the phase of the reflection coefficient has a steep excursion of about 120° across the resonance, which undergoes a spectral shift toward blue as the chemical potential of the tuning layer increases. Despite this large phase excursion, the reflectance drops across the resonance, where all the optical power is absorbed by the control layer. Conversely, when the latter is in the OFF state and the reflectance is higher than 94.9%, a full phase excursion of the reflectance coefficient is observed, with a smoother trend across the resonance wavelength. Let us define the reflection coefficient phase shift difference $\Delta\psi_{\mu c,1,\mu c,2}$ as:

$$\Delta\psi_{\mu_{c,1},\mu_{c,2}} = \psi_{\mu_{c,1},\mu_{c,2}} - \psi_{0.6,0.6} \tag{6}$$

This quantity represents the maximum difference in phase shift that a reflected wave, obtained for values of $\mu_{c,1},\mu_{c,2}\in[0.6,1]$ *eV*, can accumulate compared to a reference phase shift $\psi_{0.6,0.6}$, obtained when $\mu_{c,1}=\mu_{c,2}=0.6$ *eV*.

Figure 8(c) shows the absolute value of $\Delta\psi_{0.6,1.0}$ and $\Delta\psi_{1.0,1.0}$ as a function of the wavelength. On the one hand, when only the chemical potential of the tuning layer is raised to 1 *eV*, we observe that the maximum value of the phase shift difference reaches a value of 97.6° (see the red stem in Fig. 8(c)) is obtained at 1549.3 *nm*. Roughly the same result (98.5°) would be obtained by inverting the role of the layers (i.e., by bringing only the control layer chemical potential to 1eV and making that of the tuning layer remain at 0.6 eV). On the other hand, when both chemical potentials are raised to 1 eV, the phase shift difference reaches its maximum achievable value of about 152.5° (see the blue stem in Fig. 8(c)). This means that, by changing the chemical potential of the two graphene layers (in a non-absorbing configuration), a large phase change of the reflected electromagnetic wave is achieved at a given working wavelength, with low insertion losses, less than −0.23 *dB* in our observation domain. Finally, for the same reasons that allowed the spectral reconfigurability of the previous identified optical functions, by tuning the resonance thanks to the action of the liquid crystal, it is possible to achieve the same phase shifting behaviour throughout a 200 *nm* spectral range centred around 1550 *nm*.

## 4. Conclusion

In this manuscript, we numerically investigated the properties of an innovative multifunctional and reconfigurable 1D PhC asymmetric Fabry-Pérot cavity filled with nematic liquid crystal and bounded by two graphene monolayers. We have shown that due to the large number of degrees of freedom present in the structure, emerging in the cavity geometry and thanks to the coexistence of two different reconfigurable materials, different optical functions can be identified. We have proven that it is possible to exploit the proposed structure as a spectrally tunable notch filter (with a linewidth of 1 *nm*), due to the existence of the CPA mechanism. Furthermore, the reconfigurability of graphene conductivity allows the amount of absorption to be controlled, enabling the proposed structure to implement the function of a spectrally tunable narrowband modulator of reflected power. Finally, we have shown that when the quasi-CPA condition is not satisfied, the structure can be exploited to realize a spectrally tunable phase shifter (up to about 152° and with insertion losses lower than −0.23 *dB*, when $\mu_{c,1},\mu_{c,2}\in[0.6,1]$ *eV*), in which the chemical potential of graphene can be used to modulate the phase shift angle when they are in a non-absorbing state. In all identified functions, the orientation of the elongated molecules of the liquid crystal is exploited to achieve a spectral reconfigurability of about 200 *nm* around the working wavelength of 1550 *nm*. It is worth noting that the nematic liquid crystal is only exploited to achieve spectral reconfigurability of the different functions, while the implementation of the modulation relies on controlling the chemical potential of graphene by applying a bias, which is known to provide an ultrafast response [45]. Nevertheless, it has been demonstrated that the reorientation of the elongated molecules occurs rather rapidly (milliseconds [46], down to the ultra-fast response of 30 ns by exploiting the electric field induced modification of the order parameters (or EMOP) effect using ultra-short voltage pulses [47]). The structure presented

Optics EXPRESS

could be implemented through well-established nano- and micro-fabrication processes. The 1D-photonic crystal backbone could be fabricated by mean of radiofrequency sputtering [48,49], of standard plasma-enhanced chemical vapor deposition [50] or of e-beam evaporation [51] while graphene monolayers could be grown via Chemical Vapour Deposition and manually transferred onto the $SiO_2$ slabs. Orientation layer could be achieved via spray or spin-coating and rubbing. Finally, the electrical contacts on the side of the liquid crystal cell could be made by a standard process of optical or electronic lithography and following evaporation, while the polarization of the graphene monolayers could be realized by a coplanar side-gate scheme. It is worth mentioning that the structure, with appropriate optimization, may also be fabricated from a skeleton made from a commercial liquid crystal cell. With further research efforts aimed at identifying an optimal design of an array of independently controllable elementary cells, this powerful yet simple structure may pave the way for the realization of optical modulators and beamsteering systems.

**Funding.** Regione Puglia (Research for Innovation (REFIN)).

**Acknowledgments.** GM is supported by a grant from Regione Puglia "Research for Innovation" (REFIN). REFIN is an intervention co-financed by the European Union under the POR Puglia 2014-2020, Priority Axis OT X "Investing in education, training and professional training for skills and lifelong learning - Action 10.4 - DGR 1991/2018 - Notice 2/FSE/2020 n. 57 of 13/05/2019 (BURP n. 52 of 16/06/2019).

**Disclosures.** The authors declare no conflicts of interest.

**Data availability.** Data underlying the results presented in this paper are not publicly available at this time but may be obtained from the authors upon reasonable request.

## References

1. S. John, "Strong localization of photons in certain disordered dielectric superlattices," Phys. Rev. Lett. **58**(23), 2486–2489 (1987).
2. E. Yablonovitch and T. J. Gmitter, "Photonic band structure: The face-centered-cubic case," Phys. Rev. Lett. **63**(18), 1950–1953 (1989).
3. D. K. Armani, T. J. Kippenberg, S. M. Spillane, and K. J. Vahala, "Ultra-high-Q toroid microcavity on a chip," Nature **421**(6926), 925–928 (2003).
4. B. S. Song, S. Noda, T. Asano, and Y. Akahane, "Ultra-high-Q photonic double-heterostructure nanocavity," Nat. Mater. **4**(3), 207–210 (2005).
5. R. W. Boyd and J. E. Heebner, "Sensitive disk resonator photonic biosensor," Appl. Opt. **40**(31), 5742–5747 (2001).
6. D. Zecca, A. Qualtieri, G. Magno, M. Grande, V. Petruzzelli, B. Prieto-Simon, A. D'Orazio, M. De Vittorio, N. H. Voelcker, and T. Stomeo, "Label-free Si3N4 photonic crystal based immunosensors for diagnostic applications," IEEE Photonics J. **6**(6), 1–7 (2014).
7. C. Pin, J. B. Jager, M. Tardif, E. Picard, E. Hadji, F. De Fornel, and B. Cluzel, "Optical tweezing using tunable optical lattices along a few-mode silicon waveguide," Lab Chip **18**(12), 1750–1757 (2018).
8. M. L. Juan, M. Righini, and R. Quidant, "Plasmon nano-optical tweezers," Nat. Photonics **5**(6), 349–356 (2011).
9. B. Dagens, M. Février, P. Gogol, S. Blaize, A. Apuzzo, G. Magno, R. Mégy, and G. Lerondel, "Direct observation of optical field phase carving in the vicinity of plasmonic metasurfaces," Nano Lett. **16**(7), 4014–4018 (2016).
10. G. Calò, D. Alexandropoulos, and V. Petruzzelli, "Active photonic band-gap switch based on GaInNAs multiquantum well," IEEE Photonics J. **4**(5), 1936–1946 (2012).
11. H. Kosaka, T. Kawashima, A. Tomita, M. Notomi, T. Tamamura, T. Sato, and S. Kawakami, "Self-collimating phenomena in photonic crystals," Appl. Phys. Lett. **74**(9), 1212–1214 (1999).
12. G. Calò and V. Petruzzelli, "Wavelength routers for optical networks-on-chip using optimized photonic crystal ring resonators," IEEE Photonics J. **5**(3), 7901011 (2013).
13. K. R. Catchpole and A. Polman, "Plasmonic solar cells," Opt. Express **16**(26), 21793 (2008).
14. M. A. Green and S. Pillai, "Harnessing plasmonics for solar cells," Nat. Photonics **6**(3), 130–132 (2012).
15. G. Magno, M. Grande, A. Monmayrant, F. Lozes-Dupuy, O. Gauthier-Lafaye, G. Calò, and V. Petruzzelli, "Controlled reflectivities in self-collimating mesoscopic photonic crystal," J. Opt. Soc. Am. B **31**(2), 355 (2014).
16. G. Magno, A. Monmayrant, M. Grande, F. Lozes-Dupuy, O. Gauthier-Lafaye, G. Calò, and V. Petruzzelli, "Stable planar mesoscopic photonic crystal cavities," Opt. Lett. **39**(14), 4223 (2014).
17. A. Monmayrant, M. Grande, B. Ferrara, G. Calò, O. Gauthier-Lafaye, A. D'Orazio, B. Dagens, V. Petruzzelli, and G. Magno, "Full optical confinement in 1D mesoscopic photonic crystal-based microcavities: An experimental demonstration," Opt. Express **25**(23), 28288 (2017).
18. Z. Gong, F. Yang, L. Wang, R. Chen, J. Wu, C. P. Grigoropoulos, and J. Yao, "Phase change materials in photonic devices," J. Appl. Phys. **129**(3), 030902 (2021).

Optics EXPRESS


19. A. W. Elshaari, E. Büyüközer, I. E. Zadeh, T. Lettner, P. Zhao, E. Schöll, S. Gyger, M. E. Reimer, D. Dalacu, P. J. Poole, K. D. Jöns, and V. Zwiller, "Strain-Tunable Quantum Integrated Photonics," Nano Lett. **18**(12), 7969–7976 (2018).
20. Y. Xie, Y. Shi, L. Liu, J. Wang, R. Priti, G. Zhang, O. Liboiron-Ladouceur, and D. Dai, "Thermally-Reconfigurable Silicon Photonic Devices and Circuits," IEEE J. Sel. Top. Quantum Electron. **26**(5), 1–20 (2020).
21. C. Qiu, X. Ye, R. Soref, L. Yang, and Q. Xu, "Demonstration of reconfigurable electro-optical logic with silicon photonic integrated circuits," Opt. Lett. **37**(19), 3942–3944 (2012).
22. M. Q. Liu and C. Y. Zhao, "Reconfigurable metalattices: Combining multipolar lattice resonances and magneto-optical effect in far and near fields," J. Appl. Phys. **126**(11), 113105 (2019).
23. L. A. Falkovsky, "Optical properties of graphene," J. Phys.: Conf. Ser. **129**, 012004 (2008).
24. H. H. Radamson, "Graphene," in *Springer Handbooks*, S. Kasap and P. Capper, eds. (Springer International Publishing, 2017), **61**(3), p. 1.
25. K. Chen, R. Adato, and H. Altug, "Dual-band perfect absorber for multispectral plasmon-enhanced infrared spectroscopy," ACS Nano **6**(9), 7998–8006 (2012).
26. A. K. Jahromi, M. L. Villinger, A. El Halawany, S. Shabahang, H. Esat Kondakci, and A. F. Abouraddy, "Broadband coherent perfect absorption in graphene via an omniresonant optical microcavity," in *30th Annual Conference of the IEEE Photonics Society, IPC 2017* (2017), 2017-Janua, pp. 459–460.
27. S. Shabahang, A. K. Jahromi, L. N. Pye, J. D. Perlstein, M. L. Villinger, and A. F. Abouraddy, "Coherent perfect absorption in resonant materials," J. Opt. **23**(3), 35401 (2021).
28. K. Zhou, Q. Cheng, J. Song, L. Lu, and Z. Luo, "Highly efficient narrow-band absorption of a graphene-based Fabry–Perot structure at telecommunication wavelengths," Opt. Lett. **44**(14), 3430 (2019).
29. Y. D. Chong, L. Ge, H. Cao, and A. D. Stone, "Coherent perfect absorbers: Time-reversed lasers," Phys. Rev. Lett. **105**(5), 053901 (2010).
30. D. G. Baranov, A. Krasnok, T. Shegai, A. Alù, and Y. Chong, "Coherent perfect absorbers: Linear control of light with light," Nat. Rev. Mater. **2**(12), 17064 (2017).
31. M. A. Vincenti, D. de Ceglia, M. Grande, A. D'Orazio, and M. Scalora, "Nonlinear control of absorption in one-dimensional photonic crystal with graphene-based defect," Opt. Lett. **38**(18), 3550 (2013).
32. M. Grande, M. A. Vincenti, T. Stomeo, D. De Ceglia, V. Petruzzelli, M. De Vittorio, M. Scalora, and A. D'Orazio, "Absorption and losses in one-dimensional photonic-crystal-based absorbers incorporating graphene," IEEE Photonics J. **6**(6), 1–8 (2014).
33. P. A. Kawka and R. O. Buckius, "Optical properties of polyimide films in the infrared," Int. J. Thermophys. **22**(2), 517–534 (2001).
34. "*COMSOL Multiphysics*," www.comsol.com.
35. V. Tkachenko, G. Abbate, A. Marino, F. Vita, M. Giocondo, A. Mazzulla, F. Ciuchi, and L. De Stefano, "Nematic liquid crystal optical dispersion in the visible-near infrared range," Mol. Cryst. Liq. Cryst. **454**(1), 263/[665]–271/[673] (2006).
36. S. T. Wu and K. C. Lim, "Absorption and Scattering Measurements of Nematic Liquid Crystals," Appl. Opt. **26**(9), 1722–1727 (1987).
37. L. Gao, F. Lemarchand, and M. Lequime, "Exploitation of multiple incidences spectrometric measurements for thin film reverse engineering," Opt. Express **20**(14), 15734 (2012).
38. I. H. Malitson, "Interspecimen Comparison of the Refractive Index of Fused Silica*,†," J. Opt. Soc. Am. **55**(10), 1205 (1965).
39. C. Z. Tan, "Determination of refractive index of silica glass for infrared wavelengths by IR spectroscopy," J. Non-Cryst. Solids **223**(1-2), 158–163 (1998).
40. M. Grande, T. Stomeo, G. V. Bianco, M. A. Vincenti, D. de Ceglia, V. Petruzzelli, G. Bruno, M. De Vittorio, M. Scalora, and A. D'Orazio, "Fabrication of doubly resonant plasmonic nanopatch arrays on graphene," Appl. Phys. Lett. **102**(23), 231111 (2013).
41. L. A. Falkovsky and A. A. Varlamov, "Space-time dispersion of graphene conductivity," Eur. Phys. J. B **56**(4), 281–284 (2007).
42. G. W. Hanson, "Dyadic Green's functions and guided surface waves for a surface conductivity model of graphene," J. Appl. Phys. **103**(6), 064302 (2008).
43. R. A. Depine, "Electromagnetics of graphene," Graphene Opt. Electromagn. Solut. Canonical Probl. 1–16 (2016).
44. D. de Ceglia, M. A. Vincenti, M. Grande, G. V. Bianco, G. Bruno, A. D'Orazio, and M. Scalora, "Tuning infrared guided-mode resonances with graphene," J. Opt. Soc. Am. B **33**(3), 426 (2016).
45. J. Liu, Z. U. Khan, C. Wang, H. Zhang, and S. Sarjoghian, "Review of graphene modulators from the low to the high figure of merits," J. Phys. D: Appl. Phys. **53**(23), 233002 (2020).
46. M. A. El-Rabiaey, N. F. F. Areed, and S. S. A. Obayya, "Novel Plasmonic Data Storage Based on Nematic Liquid Crystal Layers," J. Lightwave Technol. **34**(16), 3726–3732 (2016).
47. V. Borshch, S. V. Shiyanovskii, and O. D. Lavrentovich, "Nanosecond Electro-Optic Switching of a Liquid Crystal," Phys. Rev. Lett. **111**(10), 107802 (2013).
48. A. Nematpour, N. Lisi, L. Lancellotti, R. Chierchia, and M. L. Grilli, "Experimental Mid-Infrared Absorption (84%) of Single-Layer Graphene in a Reflective Asymmetric Fabry–Perot Filter: Implications for Photodetectors," ACS Appl. Nano Mater. **4**(2), 1495–1502 (2021).

Optics EXPRESS

49. C. Williams, N. Hong, M. Julian, S. Borg, and H. J. Kim, "Tunable mid-wave infrared Fabry-Perot bandpass filters using phase-change GeSbTe," Opt. Express **28**(7), 10583 (2020).
50. B. Vosoughi Lahijani, H. Badri Ghavifekr, R. Dubey, M.-S. Kim, I. Vartiainen, M. Roussey, and H. P. Herzig, "Experimental demonstration of critical coupling of whispering gallery mode cavities on a Bloch surface wave platform," Opt. Lett. **42**(24), 5137 (2017).
51. C.-Y. Wu, Y.-H. Zou, I. Timofeev, Y.-T. Lin, V. Y. Zyryanov, J.-S. Hsu, and W. Lee, "Tunable bi-functional photonic device based on one-dimensional photonic crystal infiltrated with a bistable liquid-crystal layer," Opt. Express **19**(8), 7349 (2011).